

Supplementary Materials: In situ electric-field study of surface effects in domain engineered $\text{Pb}(\text{In}_{1/2}\text{Nb}_{1/2})\text{O}_3\text{-Pb}(\text{Mg}_{1/3}\text{Nb}_{2/3})\text{O}_3\text{-PbTiO}_3$ relaxor crystals by grazing incidence diffraction

M Cain ¹  0000-0002-8413-3104, M. Staruch ¹, P. Thompson ^{3,4}, C. Lucas ^{3,4}, D. Wermeille ^{3,4}, Y. Kayser ⁵, B. Beckhoff ⁵, S. E. Lofland ⁶ and P. Finkel, ²

1. Sample Details

- 2 The sample is a single crystal of an [011] grown [110] poled PIN-PMN-PT single crystal of
- 3 composition ~24%PIN, supplied by CTS Corporation, USA. Our sample details - see Table S1. The
- 4 sample was supplied by CTS Corporation, USA, and has nominal composition as indicated.

Sample #	Batch Number	Manufacturer	Measured k_3^T	Measured d_{32} (pC/N)	Estimated composition PIN/PMN/PT
14	WO-00476	4145	4011	1614	0.24/0.44/0.32
2	418565-1	3721	3674	1320	0.24/0.45/0.31
34	418565-1	3278	3243	1144	0.24/0.46/0.30

Table S1. Composition and some properties of samples measured in this study.

The specular surface in the chosen coordinate system of the sample is $[01\bar{1}]$ oriented, with the sample's long direction along the $[100]$ and the field parallel to $[011]$ axis. This coordinate system was not used whilst aligning and recording the diffraction contrast. The following rotational transformation, M , of axes from XMaS geometry to the aforementioned traditionally assigned coordinates was chosen:

$$M = \begin{bmatrix} 0 & 0 & 1 \\ 0 & 1 & 0 \\ -1 & 0 & 0 \end{bmatrix}$$

- 5 such that the relationship between sample geometry (s) and crystal geometry (c) is:
- 6 X1 $[01\bar{1}]_s$ is equivalent to $[110]_c$
- 7 X2 $[100]_s$ is equivalent to $[001]_c$
- 8 X3 $[011]_s$ is equivalent to $[\bar{1}10]_c$
- 9 The coordinate systems are shown in figure S1.

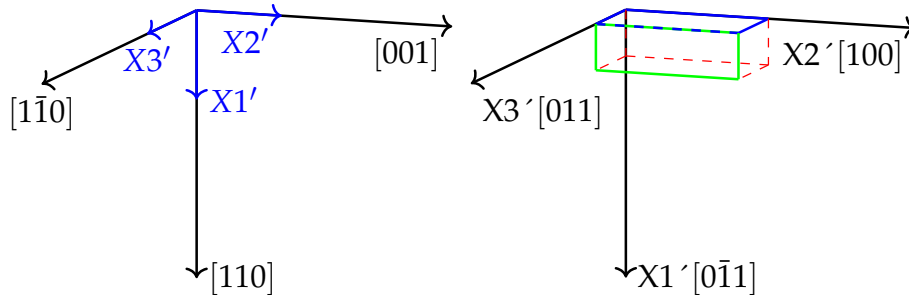


Figure S1. Two coordinate systems used in the study. Green is electroded face, and blue is specular face in right hand diagram.

11 2. Experimental details

12 The XMaS facility is a synchrotron beamline funded by the UK EPSRC research council. It is
 13 embedded in the heart of the European Photon and Neutron (EPN) Science Campus in Grenoble,
 14 France and is managed by the Universities of Liverpool and Warwick. The beamline was originally
 15 conceived in the mid-1990s primarily to perform high resolution diffraction and magnetic X-Ray
 16 scattering [1], hence the acronym X-Ray Magnetic Scattering (XMaS). The scientific areas tackled on
 17 the beamline cover a broader remit than is normally found on a single beamline, and a wide range of
 18 materials are now studied, using a variety of X-Ray techniques. Experiments are routinely performed,
 19 such as surface X-Ray diffraction [2], small/wide angle scattering (SAXS/ WAXS) measurements of
 20 soft condensed matter systems and X-Ray absorption spectroscopy (XAS) within a wide range of
 21 in-operando sample environments [3,4] and under a range of external stimuli (applied electric and
 22 magnetic fields). Although the original design specification was for a diffraction beamline, both small
 23 (SAXS) and wide angle X-ray scattering (WAXS) along with grazing incidence (GI) capabilities have
 24 been added to the operational portfolio [5].

25 The set up at the XMaS beamline is horizontal geometry Mode 4C (fourC) with the angle of
 26 incidence (α) varied between 0.01° to 0.5° , see figure S2. A six-circle 4S + 2D diffractometers (psic
 27 geometry) experimental condition with N_{az} fixed, α fixed, $\mu = \nu/2$, $N_{az} = 90$, α (incidence
 28 angle set) was chosen for the grazing incidence detection, with the diffractometer matrix set up
 29 on primary reflection (222), with secondary reflection at (330). In Grazing Incidence geometry, our
 30 diffractometer matrix had primary reflection at (223). Our lattice parameters were refined to 4.04\AA ,
 31 cubic symmetry. A single crystal cut monochromator at d-spacing 3.1333\AA with $E = 12.4\text{keV}$ yielded
 32 $\lambda = 0.999871\text{\AA}$.

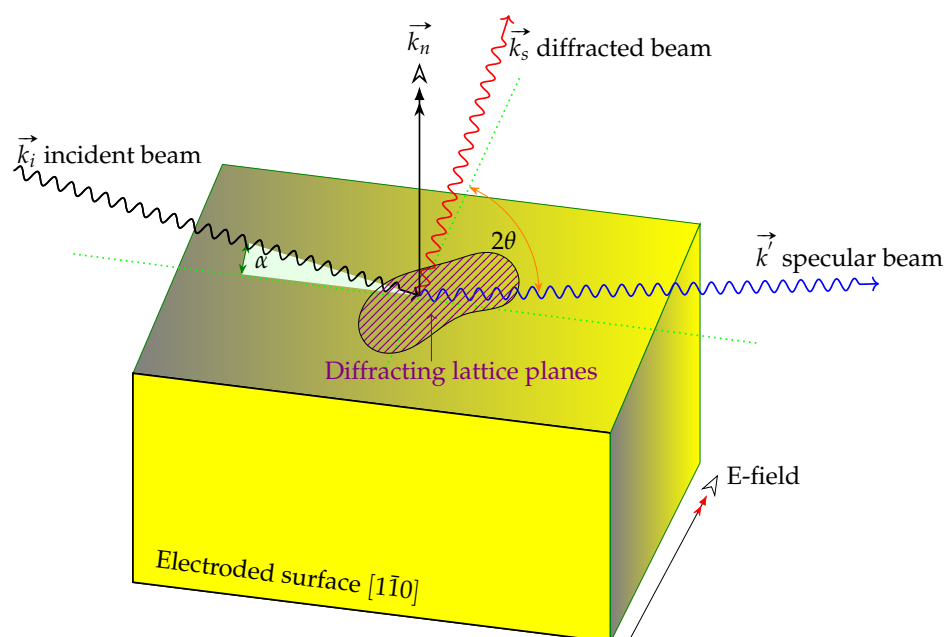


Figure S2. Grazing Incidence X-Ray diffraction for PIN-PMN-PT, with grazing incidence angle denoted by α , and diffraction conditions in horizontal geometry given by the usual 2θ .

33 Sample electrodes were evaporated gold, deposited onto the $[1\bar{1}0]$ faces (perpendicular to the
 34 sample surface normal), see figure S1 and figure 1a (main paper) for more details of sample orientation
 35 and figure S2 for diffraction configuration. After the surfaces are ground and polished to $\sim 1/4\mu\text{m}$, the
 36 sample is mounted using low melting temperature wax onto an insulating substrate. High voltage
 37 wiring is affixed to the sample jig, and routed out of the diffractometer using high voltage S-BNC
 38 cables, to a TREK 610E HV amplifier (TREK Inc. Lockport, New York 14094 USA). Details are provided
 39 in reference [4], and shown in figure S3. The TREK was set at its 10kV output range and its monitor

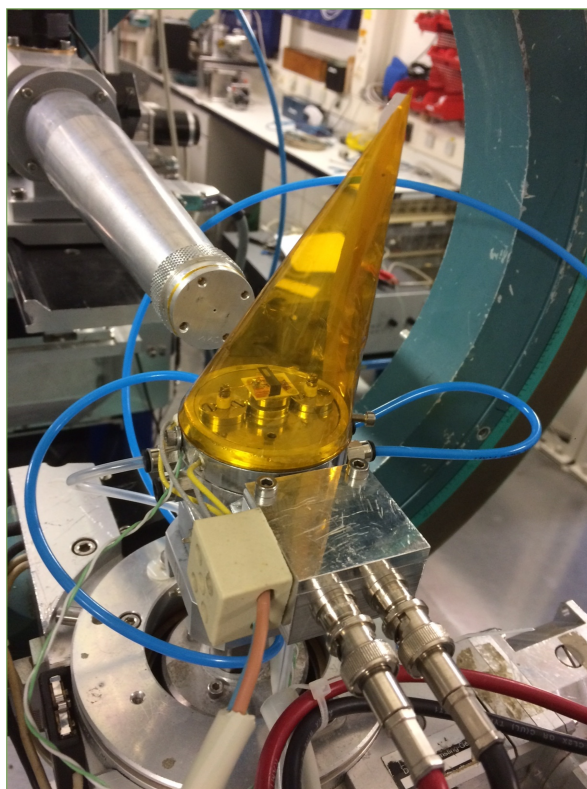


Figure S3. Sample and fixture assembled and attached to the goniometer, set with a heating stage. Note Kapton tent providing both safety barrier to high voltages and also ability to present a dry nitrogen atmosphere around the sample.

40 signal (1/1000 output voltage) was recorded. The high voltage amplifier safely connects to the high
41 voltage coaxial cables and is interlocked with the beamline hutch.

42 The setup within the XMaS SPEC software UB Matrix (U-rotation matrix describing the orientation of
43 the crystal in the laboratory frame, B - an orthogonalisation matrix, which defines a set of orthogonal
44 axes based on the crystal axes, so the UB matrix defines how the crystal is oriented with respect to
45 the laboratory coordinate system), assumed a pseudo cubic symmetry of the bulk single crystal, with
46 a priori knowledge that these crystals take rhombohedral, orthorhombic and tetragonal symmetries
47 under E-field and monoclinic variants at all other times.

48 The advantages of using a synchrotron over a laboratory-based X-Ray system is an increase of at least 3
49 orders of magnitude signal to noise and hence reduction in counting times per reciprocal lattice image
50 using the 2D Pilatus3 300K detector.

51 The experimental methodology proceeded through triangular wave excitation of the sample to \pm
52 1500V applied to the 4mm wide sample creating a field of $\pm 3.75\text{kV/cm}$, whilst recording current,
53 strain and X-Ray counts as described. In-plane strain is measured using a strain gauge affixed to the
54 specular surface with strain direction along the long (001) sample direction. Attachment of the strain
55 gauge (RS Pro 2.5mm gauges $120\ \Omega$ 632-146) to the single crystal was carried out using cyanoacrylate
56 adhesive, leaving sufficient space for the X-Ray beam off this specular surface. Fixation of strain
57 gauges must be carefully performed to make sure that good strain transfer exists from the cleaned
58 sample surface and the strain gauge backing material, see figure S4. The strain is then measured using
59 a Honeywell strain gauge amplifier in 3 wire setup to eliminate effects of temperature on resulting
60 strain measured. Calibration is carried out using a 1% tolerance shunt resistor circuit.

61 A large number of PILATUS3 X 300K reciprocal maps were recorded for each experimental parameter,
62 and the centroid of the peak in each was automatically measured using code written in IDL with
63 the pixel coordinate converted to (HKL) and plotted as HKL with field, strain with field (assuming

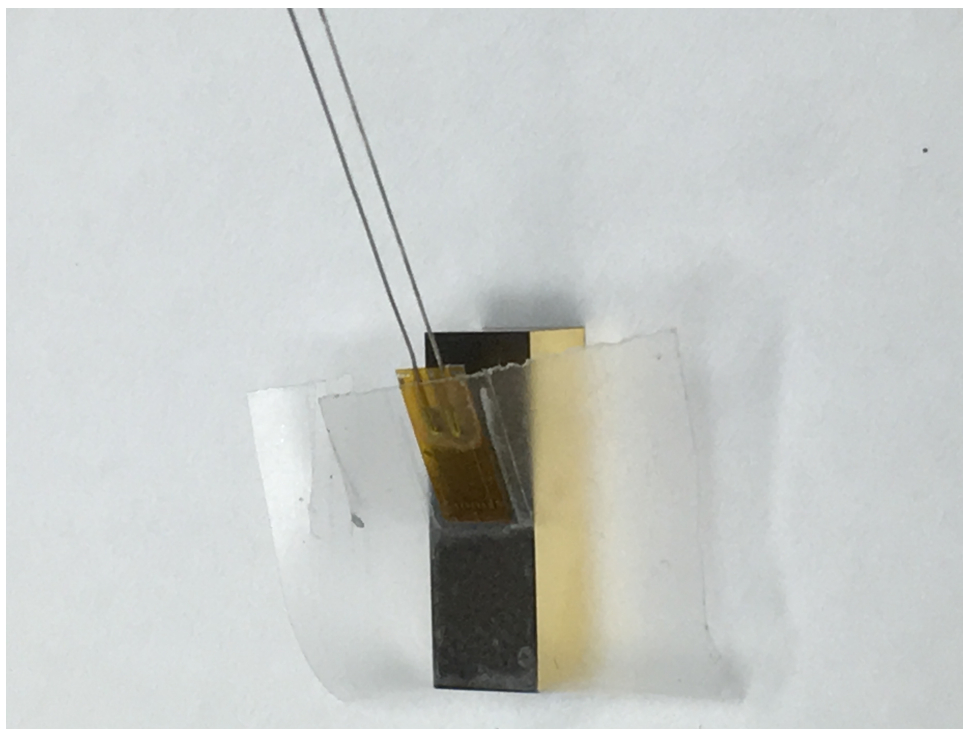


Figure S4. Attachment of the strain gauge (RS Pro 2.5mm gauges 120 Ω 632-146) to the single crystal using cyanoacrylate adhesive, leaving sufficient space for the X-Ray beam off this specular surface.

64 pseudo cubic symmetry) and effective piezoelectric coefficients with depth through the specular
65 surface. Procedure: (see also Figure 2 in main paper): From image analysis \rightarrow peak position locus \rightarrow
66 HKL conversion \rightarrow (see figure S5), lattice parameter based strain calculation \rightarrow strain through depth
67 calculation (figure S10). During this process, data is interpolated only once within the HKL conversion
68 process.

69 The HKL plot in figure S5 shows a) a 2D Pilatus image of the (010) reflection, in pixel coordinates
70 alongside its b) HKL coordinate reference frame, demonstrating the conversion algorithms used in this
71 study, and the approximate orientation of the camera with respect to the sample crystallography, with
72 y-axis \sim [110] and x-axis \sim [1.10]. The detector was placed at a distance \sim 1m away from the sample,
73 resulting in a very large field of view in HK space, necessitating the use of Region of Interest zooming
74 algorithms to better define the changes in peak position of the reflection as a function of electric field.
75 The variation in L is less than 0.01 \AA , for L = 0 nominal across the whole scan. The errors introduced
76 by the assumption that L is invariant and analysis of raw data using zooming interpolation are less
77 than 2% in HKL, though future experimental statistics would be improved by moving the detector
78 closer to the sample, and carrying out full 3D volume imaging, rather than this thin slice of 3D space.
79 The data in figure S5 is at zero applied volts, $\alpha = 0.1^\circ$ at 40 $^\circ\text{C}$. The spread of X-Ray intensity along
80 approx. direction (110) is due to variations in the in-plane lattice parameter (010) arising, possibly
81 from surface roughness [6], though primarily from the low angle of incidence of the interrogating
82 X-Rays. The surface strains in the single crystal would yield a variation in interplanar spacing in both
83 parallel and perpendicular directions with respect to the specular surface, through Poisson's ratio. The
84 response from the (010) planes would suggest a significant variation in the [HH0] spacing compared
85 to the orthogonal [0K0] direction would be observed, which is exactly what is observed in figure S5.
86 The data presented in the figures S6- S9 examines the changes in position of centroid peak of all four
87 reflections as a function of electric field (calculated as strain in these graphs), at a temperature of 40 $^\circ\text{C}$
88 at $\alpha \sim 0.5\text{-}0.5^\circ$, to demonstrate the data analysis approach: From image analysis \rightarrow peak position locus
89 \rightarrow HKL conversion \rightarrow (see figure S5a), lattice parameter based strain calculation \rightarrow strain through

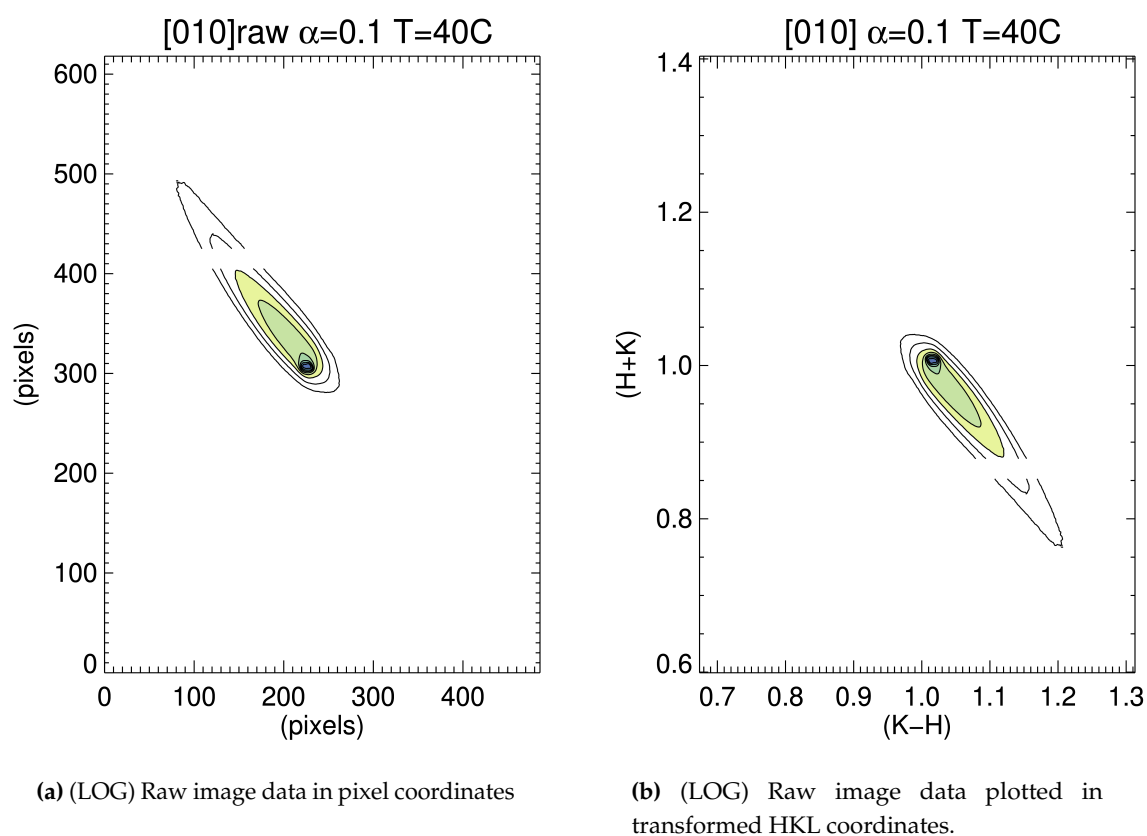


Figure S5. A H-K reciprocal space contours Our data is taken using full 2D X-Ray images (Pilatus 300k camera) allowing us to very rapidly explore the nature of competing crystallographic transformations arising across quite a large reciprocal space, here centered on (010). The strip spanning the horizontal axis hides the data at those HKL values, and is associated with the internal detector arrays of the Pilatus camera, which does not impact this data analysis.

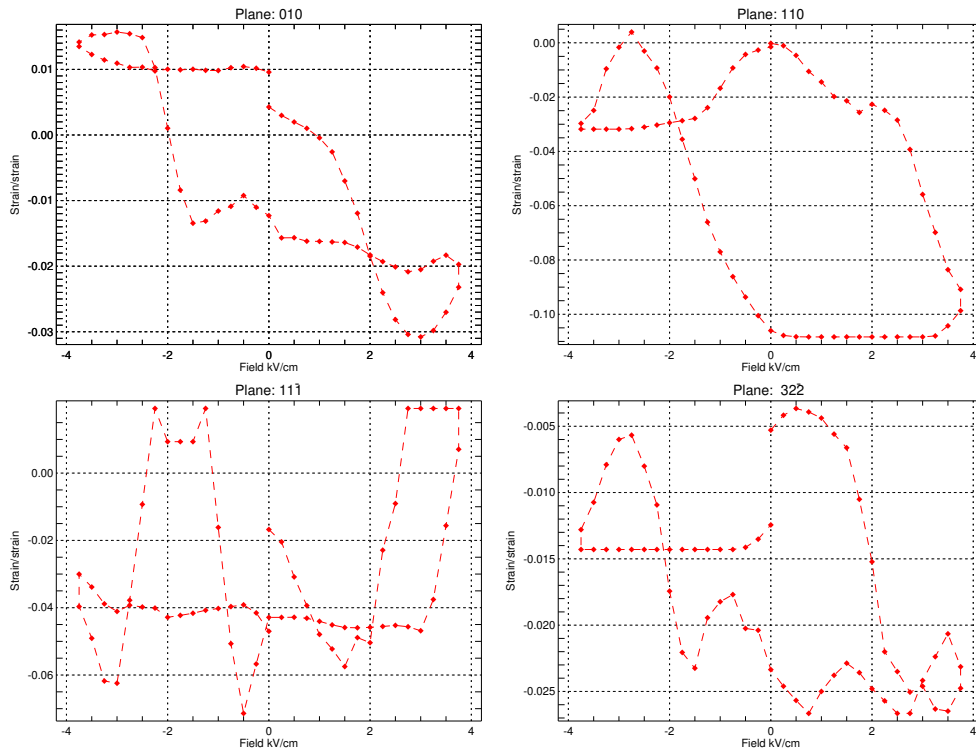


Figure S6. X-Ray derived Strain measured as a function of electric field for all grazing incidence reflections, at 40°C, for $\alpha = 0.1^\circ$, showing the complex ferroelectric switching strain field response with asymmetrical hysteresis within the surface of the single crystal sample.

90 depth calculation (see main paper). During this process, data is interpolated only once within the HKL
 91 conversion process.

92 3. Grazing Incidence and penetration of X-Rays into solids

The degree of penetration of X-Rays into a solid depends on energy of the radiation, geometrical factors and sample parameters[6,7], and is in general a complex form of Snell's law based on the refractive index of a medium for X-Rays, according to equation 1:

$$n = 1 - \delta - i\beta \text{ with } \delta = \frac{2\pi\tau_0\rho}{|k|^2} \text{ and } \beta = \frac{\mu}{2|k|} \quad (1)$$

with ρ electronic density, τ_0 classical electron radius= $2.818 \times 10^{-5} \text{ \AA}$, μ linear absorption coefficient and $|k|$ length of incident wave vector ($=2\pi/\lambda$), which may be used in the following equation governing penetration depth, Λ , of X-Rays:

$$\Lambda = \frac{1}{2k\Im(\alpha')} \quad (2)$$

93 with α =angle of incidence and \Im signifies its Imaginary component. The response, for
 94 X-Ray Energy=12.4keV chosen in this experiment, is shown for average elemental composition
 95 $\text{Pb}(\text{In}_{1/2}\text{Nb}_{1/2})\text{O}_3$ - $\text{Pb}(\text{Mg}_{1/3}\text{Nb}_{2/3})\text{O}_3$ - PbTiO_3 , in figure S10.

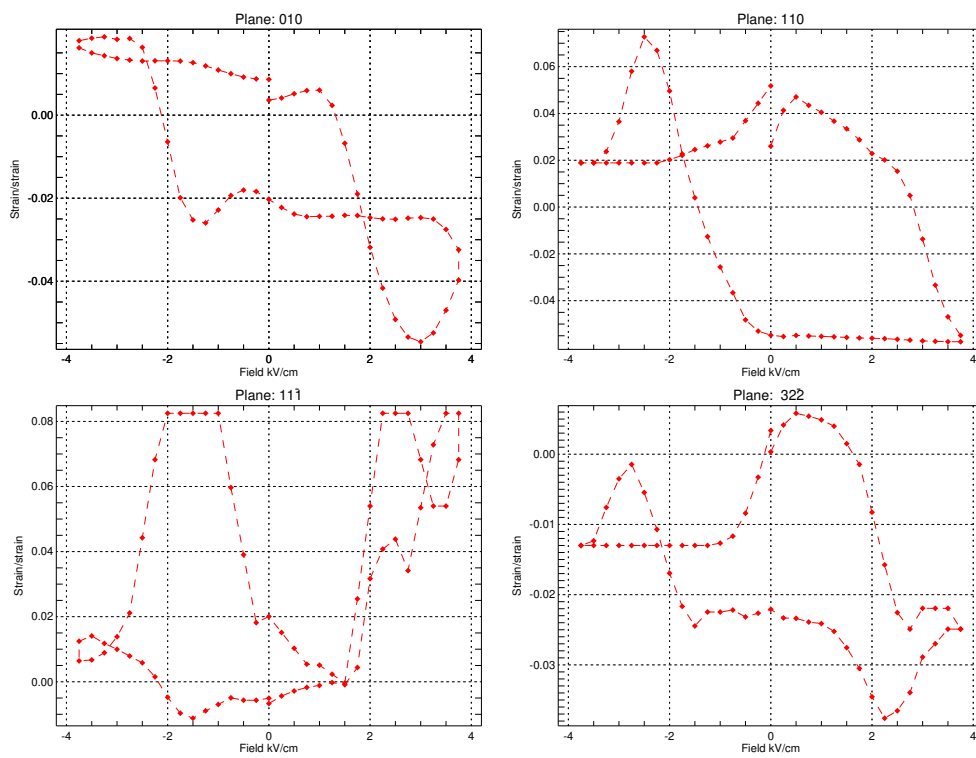


Figure S7. X-Ray derived Strain measured as a function of electric field for all grazing incidence reflections, at 40°C, for $\alpha = 0.2^\circ$, showing the complex ferroelectric switching strain field response with asymmetrical hysteresis within the surface of the single crystal sample.

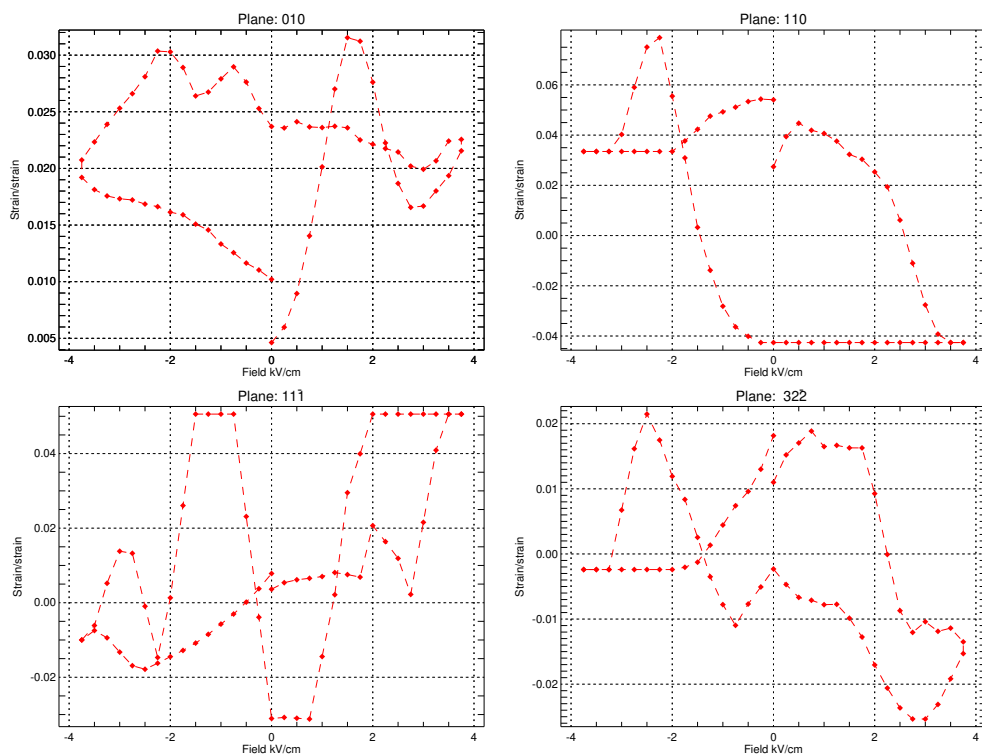


Figure S8. X-Ray derived Strain measured as a function of electric field for all grazing incidence reflections, at 40°C, for $\alpha = 0.3^\circ$, showing the complex ferroelectric switching strain field response with asymmetrical hysteresis within the surface of the single crystal sample.

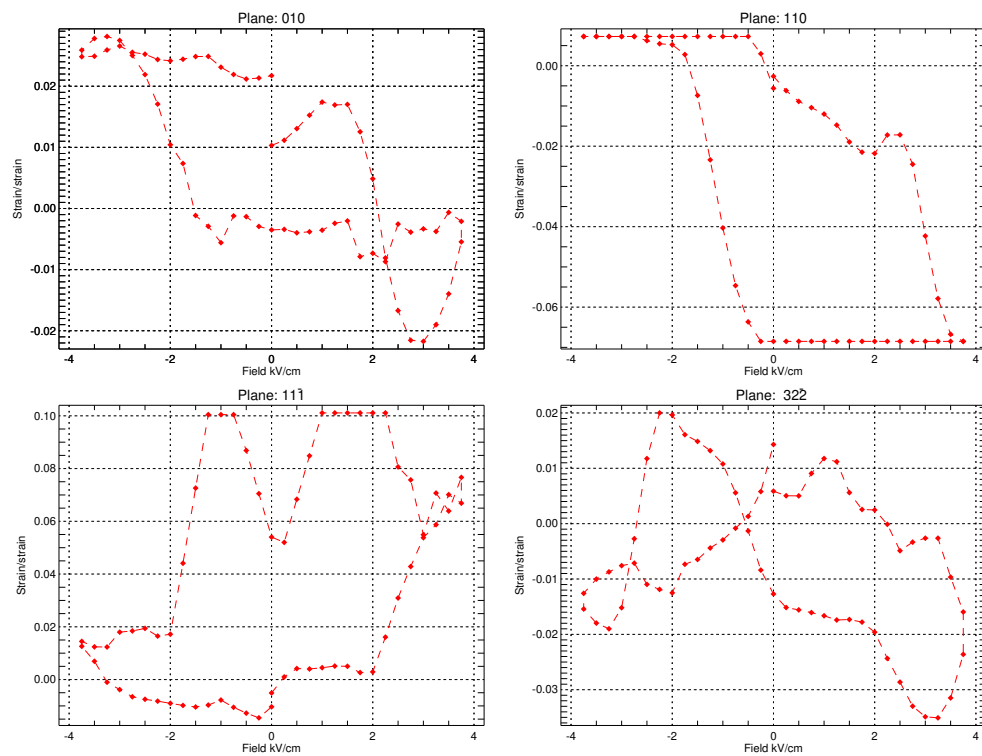


Figure S9. X-Ray derived Strain measured as a function of electric field for all grazing incidence reflections, at 40°C, for $\alpha = 0.5^\circ$, showing the complex ferroelectric switching strain field response with asymmetrical hysteresis within the surface of the single crystal sample.

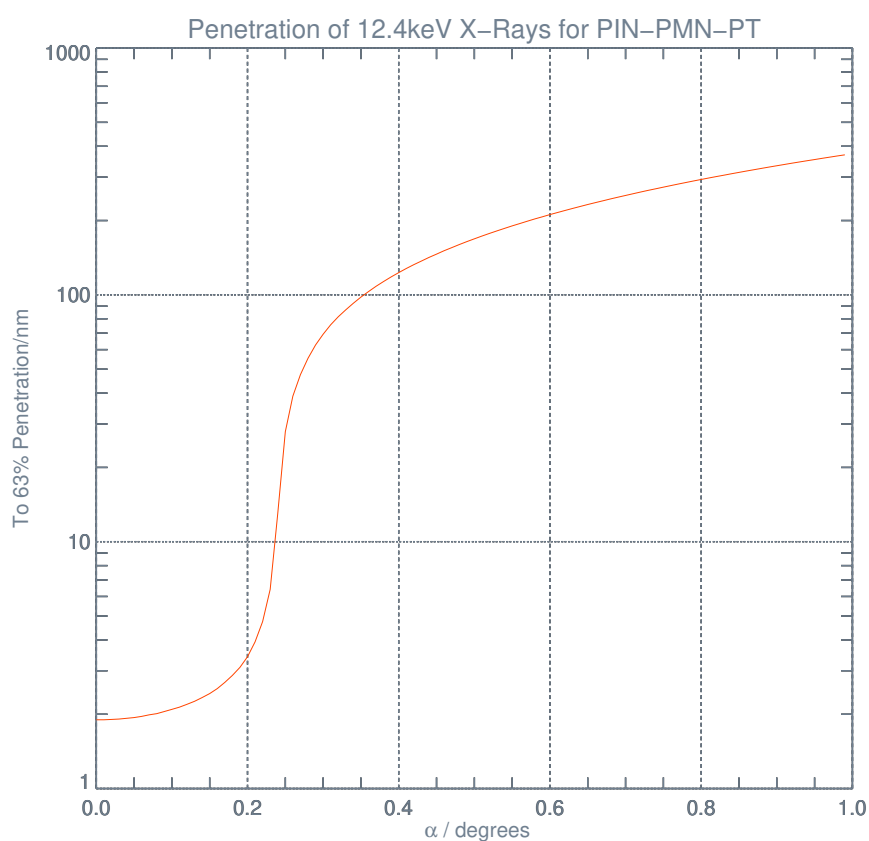


Figure S10. Calculation of the penetration depth of X-Rays at $E=12.4\text{keV}$, into PIN-PMN-PT average elemental composition as a function of grazing incidence angle, α . The graph shows as a LOG plot, the corresponding penetration depth of X-Rays, such that $\sim 63\%$ of emitted X-Rays originate from that sample depth defined by the penetration angle in degrees on the x-axis.

96

- 97 1. Brown, S.D.; Bouchenoire, L.; Bowyer, D.; Kerwin, J.; Laundry, D.; Longfield, M.J.; Mannix, D.; Paul,
98 D.F.; Stunault, A.; Thompson, P.; Cooper, M.J.; Lucas, C.A.; Stirling, W.G. The XMaS beamline at ESRF:
99 instrumental developments and high-resolution diffraction studies. *Journal of Synchrotron Radiation* **2001**,
100 *8*, 1172–1181.
- 101 2. Lucas, C.A.; Thompson, P.; Cormack, M.; Brownrigg, A.; Fowler, B.; Strmcnik, D.; Stamenkovic, V.; Greeley,
102 J.; Menzel, A.; You, H.; Marković, N.M. Temperature-Induced Ordering of Metal/Adsorbate Structures at
103 Electrochemical Interfaces. *Journal of the American Chemical Society* **2009**, *131*, 7654–7661.
- 104 3. Wooldridge, J.; Ryding, S.; Brown, S.; Burnett, T.L.; Cain, M.G.; Cernik, R.; Hino, R.; Stewart, M.; Thompson,
105 P. Simultaneous measurement of X-ray diffraction and ferroelectric polarization data as a function
106 of applied electric field and frequency. *Journal of Synchrotron Radiation* **2012**, *19*, 710–716.
- 107 4. Vecchini, C.; Thompson, P.; Stewart, M.; Muniz-Piniella, A.; McMitchell, S.R.C.; Wooldridge, J.; Lepadatu,
108 S.; Bouchenoire, L.; Brown, S.; Wermeille, D.; Bikondoa, O.; Lucas, C.A.; Hase, T.P.A.; Lesourd, M.; Dontsov,
109 D.; Cain, M.G. Simultaneous dynamic electrical and structural measurements of functional materials.
110 *Review of Scientific Instruments* **2015**, *86*, 103901–10.
- 111 5. Bikondoa, O.; Bouchenoire, L.; Brown, S.; Thompson, P.; Wermeille, D.; Lucas, C.A.; Cooper, M.; Hase, T.
112 XMaS @ the ESRF. *Philosophical Transactions A* **2019**, pp. 1–13.
- 113 6. Jordan Sweet, J.L.; Mooney, P.M.; Lutz, M.A.; Feenstra, R.M.; Chu, J.O.; LeGoues, F.K. Unique x-ray
114 diffraction pattern at grazing incidence from misfit dislocations in SiGe thin films. *Journal of Applied Physics*
115 **1996**, *80*, 89–96.
- 116 7. Fuoss, P.H.; Brennan, S. Surface sensitive X-ray scattering. *Annual review of materials science* **1990**,
117 *20*, 365–390.